J Mater Sci (2022) 57:217–228

Ceramics

Optimization of energy-storage properties for lead-free relaxor-ferroelectric (1-x)$Na_{0.5}Bi_{0.5}TiO_3$-x$Sr_{0.7}Nd_{0.2}TiO_3$ ceramics

Ziyue Ma[1], Qian Su[1], Jianye Zhu[1,2], Xiangjun Meng[1], Ye Zhao[1,2], Guoxiang Xin[3], Yong Li[1,*], and Xihong Hao[1,*]

[1] *Inner Mongolia Key Laboratory of Ferroelectric-Related New Energy Materials and Devices, School of Materials and Metallurgy, Inner Mongolia University of Science and Technology, Baotou 014010, China*

[2] *Key Laboratory of Integrated Exploitation of Bayan Obo Multi-Metal Resources, Inner Mongolia University of Science and Technology, Baotou 014010, China*

[3] *School of Materials and Metallurgy, Inner Mongolia University of Science and Technology, Baotou 014010, China*

Received: 20 July 2021
Accepted: 27 October 2021
Published online: 3 January 2022

ABSTRACT

Ferroelectrics are considered as the most promising energy-storage materials applied in advance power electronic devices due to excellent charge–discharge properties. However, the unsatisfactory energy-storage density is the paramount issue that limits their practical applications. In this work, the excellent energy-storage properties are achieved in (1-x)$Na_{0.5}Bi_{0.5}TiO_3$-x$Sr_{0.7}Nd_{0.2}TiO_3$ ((1-x)NBT-xSNT) ferroelectric ceramics by a synergistic strategy, where SNT improves breakdown strength and enhances relaxation characteristic simultaneously. A high recoverable energy-storage density of 3.85 J cm^{-3} and an energy-storage efficiency of 85.3% under an applied electric field of 305 kV cm^{-1} are acquired in 0.5NBT-0.5SNT ceramic. Moreover, excellent temperature stability and frequency stability were also observed. The change rate of energy density is less than 10%, where the temperature and frequency in the range of 20–120 °C and 20–180 Hz, respectively. Meanwhile, an ultrahigh power density of 175 MW cm^{-3} together with a fast discharge time of 136 ns is realized at 250 kV cm^{-1}. These excellent performances show that (1-x)NBT-xSNT ceramics have the potential to be used in pulsed power systems.

Handling Editor: David Cann.

Address correspondence to E-mail: liyong3062545@126.com; xhhao@imust.cn

https://doi.org/10.1007/s10853-021-06684-6

Introduction

With the rapid development of new materials and energy conversion as well as storage devices in pulsed power systems, advanced function materials have been brought into focus [1–9]. Ceramic-based dielectric materials have been receiving considerable attentions because of fast charge–discharge speed, ultra-high power density and excellent stability [10, 11]. In general, four typical dielectric ceramics are suited for energy-storage application, including linear dielectrics (LDs), ferroelectrics (FEs), antiferroelectrics (AFEs) and relaxation ferroelectrics (RFEs) [4, 5, 12–14]. Linear dielectric ceramics have high energy-storage efficiency (η) due to tiny remnant polarization (P_r), but low maximum polarization (P_{max}) limits their recoverable energy-storage density (W_{rec}). For instance, $Ca_{0.5}Sr_{0.5}Ti_{0.9}Zr_{0.1}O_3$ ceramic exhibits a large η (97%), but the W_{rec} is just 2.05 J cm^{-3} [15]. Ferroelectric ceramics are another class of attractive candidates for energy-storage due to the high polarization. However, the shortcoming is high P_r, leading to a large energy-storage loss (W_{loss}) during the phase transition and domain wall motion [16–18]. Antiferroelectric ceramics have good energy-storage properties owing to large P_{max} and small P_r. Nonetheless, double hysteresis loops and antiferroelectric-paraelectric phase transition led to a small energy-storage efficiency and temperature-sensitive energy-storage, respectively [5, 19–21]. Nowadays, relaxor ferroelectric ceramics as the potential energy-storage materials have attracted a lot of interests. Due to the order-disordering of cations and the random electric fields (RFS), long-range domains of relaxation materials are disrupted at the nanoscale and polar nano-regions (PNRs) are created [22], thereby leading to a slender polarization–electric field (P-E) hysteresis loops together with high electric displacement, excellent stability performance, high power density and fast charge–discharge rates [23].

Among relaxor ferroelectric ceramics, $Na_{0.5}Bi_{0.5}TiO_3$ (NBT)-based ceramics are considered to be the most competitive lead-free candidate materials owing to high P_{max} (43 μC cm^{-2}). However, low breakdown strength (BDS) and small hysteresis characteristics lead to low W_{rec} [24–26]. Therefore, many studies have been carried out to improve relaxation behavior of NBT-based ceramics, resulting in an enhancement in the energy-storage density. As reported by Yan et al., introducing Sr^{2+} ion and $(Al_{0.5}Nb_{0.5})^{4+}$ complex-ion into BNT ceramic to disrupt the long-range ordering of ferroelectrics and induce the generation of PNRs. The energy-storage properties of (1-x)$Bi_{0.5}Na_{0.5}TiO_3$-x$SrNb_{0.5}Al_{0.5}O_3$((1-x)BNT-xSNA) RFE ceramics were increased via inducing the PNRs to decrease the P_r and decreasing the grain size to submicron scale to improve the relaxation behavior and BDS [27]. Qiao et al. prepared (1-x)$Bi_{0.5}Na_{0.5}TiO_3$-x$Sr_{0.7}La_{0.2}TiO_3$ ((1-x)BNT-xSLT) RFE ceramics, exhibiting a large BDS of 338 kV cm^{-1} due to grain size reduction, in addition to enhanced relaxation behaviors by driving Ts to room temperature. [28]. It is of great significance to combine fined grains and high densification to enhance BDS and relaxation behavior of NBT-based RFEs, resulting in further improved performances for practical applications [29–31].

In this study, high energy-storage density and efficiency are achieved in (1-x)$Na_{0.5}Bi_{0.5}TiO_3$-x$Sr_{0.7}Nd_{0.2}TiO_3$ ((1-x)NBT-xSNT) ceramics by the addition of SNT. SNT exhibits an obvious effect on decreasing gain size and domain size, leading to the enhancement of BDS and relaxation behavior. And (1-x)NBT-xSNT ceramics were manufactured by the tape-casting method for improving the microstructure and densification of the ceramics, which effectively improves the BDS of ceramics and helps to achieve the desired energy-storage properties [20, 32, 33]. As a result, the excellent energy-storage property is obtained at a high electric filed. These excellent performances confirm the potential of the NBT-based ceramics for dielectric capacitors in advanced power electronic devices and pulsed power systems.

Experimental details

RFE ceramics of the (1-x)NBT-xSNT (x = 0.2, 0.3, 0.4 and 0.5) ceramics were prepared by tape-casting technique and sintered via traditional solid-state reaction method. Firstly, the Na_2CO_3 (99.8%), Bi_2O_3 (99.0%), TiO_2 (98.0%), $SrCO_3$ (99%) and Nd_2O_3 (99.9%) were weighted according to the stoichiometric ratio and ball-milled (QM-3SP2, Nanjing University Instrument Factory, China) in ethanol for 24 h as the raw powders. The raw powders were dried and calcined at 850 °C for 4 h. The calcined powders were ball-milled again for 24 h. Secondly, ethyl alcohol, tributyl phosphate, Polyvinyl Butyral (PVB) binder

and Plasticiser (Polyethylene glycol, Phthalate) were added to the ceramic powders, then mixture were ball-milled for 18 h to obtain tape-casting slurry. It took 25 min to remove the bubbles from the tape-casting slurry by a vacuum defoaming machine (TP-08, Beijing Orient Sun-Tec Co. Ltd., China). The slurry was cast on a film-belt substrate with the help of a continuous tape-casting machine (LY-150, Beijing Orient SunTec CO. Ltd., China). The obtained thick film was stacked together (DY-30, Tianjin Science and Technology Co. Ltd., China) and disposed under a high pressure to further densify the green-samples via a cold isostatic pressure technique (U150, Shanxi Golden Kaiyuan Co., Ltd. China). The samples were calcined at 500 °C to burn out the binder and sintered at 1170 °C for 3 h in the crucibles. In order to avoid the evaporation of Na^{+}, Bi^{3+} in the high-temperature sintering process, the samples were embedded in the calcined powders of the same composition. Finally, the ceramic samples were polished to 100 μm and sputtered with an electrode area of 3.14 mm^2 before electrical performances tests.

The phase structures of NBT-SNT ceramics were performed by an X-ray diffractometer (Bruker D8 Advanced Diffractometer, German). The surface morphology of the ceramics was observed by a scanning electron microscopy (FE-SEM, ZEISS Supra 55, German). The relative density of the ceramics was calculated by the Archimedes drainage method. The domains and piezoresponse loops were measured by a piezoelectric force microscope (PFM, Bruker, Icon). Temperature dependence of the relative permittivity (ε_r) and dielectric loss ($tan\delta$) was detected via a computer-controlled LCR meter (TH2828, Tonghui, China). The P-E hysteresis loops at the frequency of 10 Hz were measured by a ferroelectric test system (Radiant Technologies, Inc., Albuquerque, USA). The pulsed discharge current was characterized via the RLC circuit (CFD-001, Guoguo technology, China) and recorded by an oscilloscope (TBS 1102B-EDU, Tektronix CO., China).

Results and discussion

The room-temperature XRD patterns of (1-x)NBT-xSNT ceramics are characterized in Fig. 1a. All ceramics exhibit pure perovskite structure with no apparent trace of the secondary phase [24, 34]. Furthermore, the (111) and (200) peaks gradually move toward the higher angles as the concentration of SNT increases, as depicted in Fig. 1b. It implies a contraction of lattice constant due to the replacement of Na^{+} (1.02 Å) ions and Bi^{3+} (1.03 Å) ions by the smaller Nd^{3+} (0.983 Å) ions [16, 24, 35].

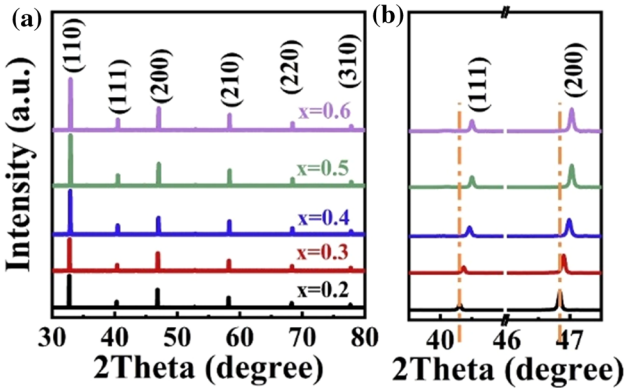

Figure 1 (**a**) X-ray diffraction patterns of (1-x)NBT-xSNT ceramics in a wide range from 30° to 80°; (**b**) The spectra were magnified at (111) and (200) peaks.

Figure 2 shows the SEM images and the grain size distribution of (1-x)NBT-xSNT ceramics. The relative densities of (1-x)NBT-xSNT ceramics are also calculated, which are 94.9, 96.1, 96.5, 96.7 and 97.3%, respectively. It is found that the ceramic of $x = 0.2$ exhibits a loose microstructure with a lot of pores. With the content of SNT increasing, the densification of the ceramics increases and the pores disappear. Moreover, based on SEM images, the size of 200 grains is counted by the Nano Measurer software to obtain the grain size distribution [35, 36], the average grain size reduces from 2.53 to 0.96 μm when x increases from 0.2 to 0.6, and the distribution of grain size is more uniform. The small grain size and dense structure are beneficial to gain high BDS verified by previous reported [28, 37].

Figure 3a–e shows the out-of-plane phase PFM images of (1-x)NBT-xSNT ceramics. The clear long-range ordered FE domains can be observed in the $x = 0.2$ sample (Fig. 3a). The polarization direction of the bright regions is opposite to the dark regions, where the bright regions and the dark regions represent upward and downward polarization, respectively [38]. The complete ferroelectric domain structure of $x = 0.2$ sample is illustrated by the alternating bright and dark regions. It can be found that the increase of SNT content has made the contrast in PFM images become blurred. FE domains gradually become smaller and more irregular. This is

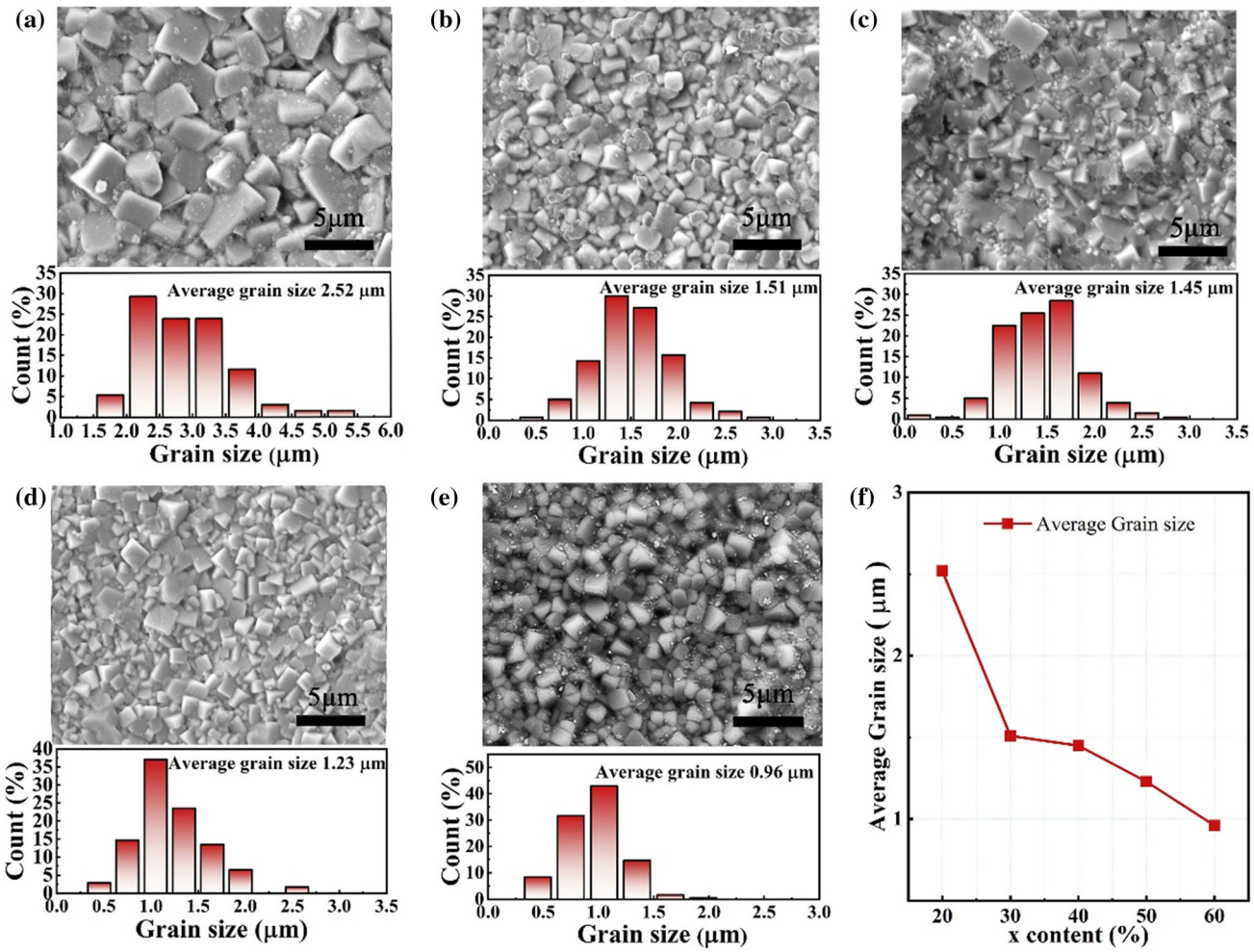

Figure 2 SEM images and grain size distribution of (1-x)NBT-xSNT ceramics: (**a**) $x = 0.2$, (**b**) $x = 0.3$, (**c**) $x = 0.4$, (**d**) $x = 0.5$, (**e**) $x = 0.6$; (**f**)The average grain size of (1-x)NBT-xSNT ceramics.

due to the local RFS created by the introduction of SNT in the NBT, which is caused by structural and charge inhomogeneity around the substitution ions. The presence of local RFS has been widely reported to hinder long-range ordering and produce PNRs [39]. It is indicated that the introduction of SNT decreases the size of domains and gives rise to PNRs [39, 40]. To obtain deeper insight into the behavior features of domain structure, the piezo response loops on selected regions of all samples are also carried out. It is found that the FE domains give saturated square-shaped phase loops, whereas the PNRs show pinched loops. In short, the addition of SNT to the NBT matrix indicates that the long-range order of FE domains is disrupted and leads to the appearance of PNRs, thereby resulting in a structure transformation from FE to RFE.

The temperature dependence of ε_r and $tan\delta$ for (1-x)NBT-xSNT ceramics was measured at the different frequencies of 1 kHz-1 MHz is depicted in Fig. 4a–e. The tanδ decreases and then increases at higher temperatures. It is attributed to the oxygen vacancies getting activated at a higher temperature, resulting in increased conductivity [41]. Two dielectric peaks are observed according to the curves, including the absolute maximum dielectric peak (T_m) and a low-temperature peak (T_s). For the NBT-based ceramics, the dielectric anomaly at T_s is attributed to the thermal evolution of the PNRs of rhombohedral (R3c) and tetragonal (P4bm) structured. T_m is related to a mixed contribution from the transition of PNRs from R3c to P4bm structured and a thermal evolution of PNRs [2, 24, 33, 42–44]. Furthermore, the ε_r and tanδ exhibit an obvious frequency dispersion around T_s. Due to the occupation of the $(Na_{0.5}Bi_{0.5})^{2+}$ by the

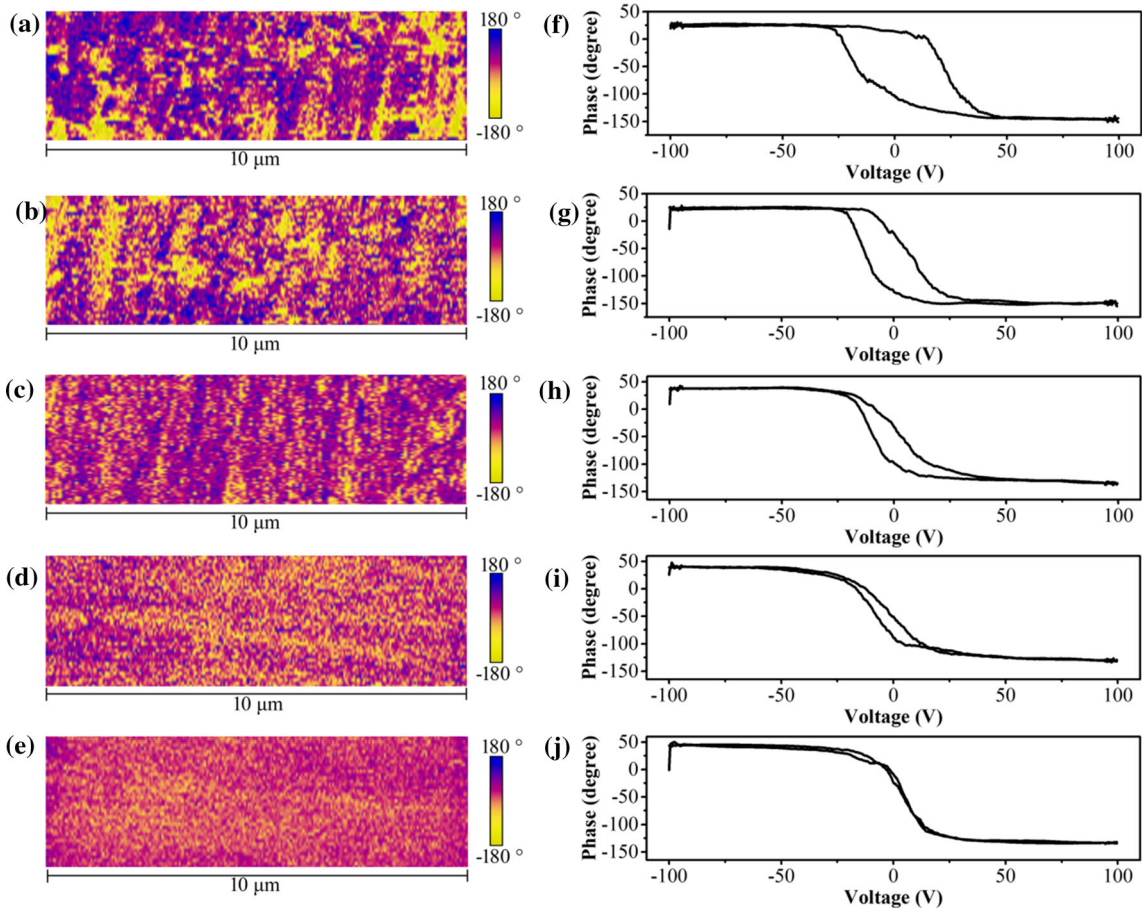

Figure 3 Out-of-plane PFM images and piezoresponse phase of (1-x)NBT-xSNT ceramics phase: (**a**, **f**) $x = 0.2$, (**b**, **g**) $x = 0.3$, (**c**, **h**) $x = 0.4$, (**d**, **i**) $x = 0.5$, (**e**, **j**) $x = 0.6$.

Nd^{3+}, the differences in radius and valence of these cations at A-site give rise to enhance RFS. It can produce a competition between the long-range driving dipoles and the translational symmetry, which tends to enhance the RFS. The PNRs generated by local random bonds that will give rise to typical relaxation properties [45]. T_s, T_m and the maximum relative permittivity (ε_m) gradually decrease with the content of SNT increasing, as shown in Fig. 4f. This result suggests the deformation of local lattice and destruction of ferroelectric long-range order with the content of SNT increasing, inducing the RFS. The RFS resulting in a gradual increase in the dynamics of PNRs and thus can enhance the relaxor behavior [2, 41].

To characterize the BDS of the ceramics, the Weibull distribution is acquired based on eight samples of every ceramic. The Weibull distribution can be calculated by the equations:

$$X_i = \ln(E_i) \tag{1}$$

$$Y_i = \ln\left(\ln\left(1/(1-\frac{i}{n+1})\right)\right) \tag{2}$$

where E_i and n represent the values of specimens and the group number of test ceramics, respectively [42]. The results for the Weibull distribution of (1-x) NBT-xSNT ceramics are shown in Fig. 5a. The graph shows a good fit of the data points, and all shape parameters (β) are higher than 13 for each composition [27, 30]. The breakdown data of all samples follow a good agreement with the Weibull distribution. The BDS of the ceramics is shown in Fig. 5b. The BDS increases from 140 to 320 kV cm^{-1} with the increase of the x from 0.2 to 0.6. The relationship between BDS and grain size (G) is computed by using the following relations:

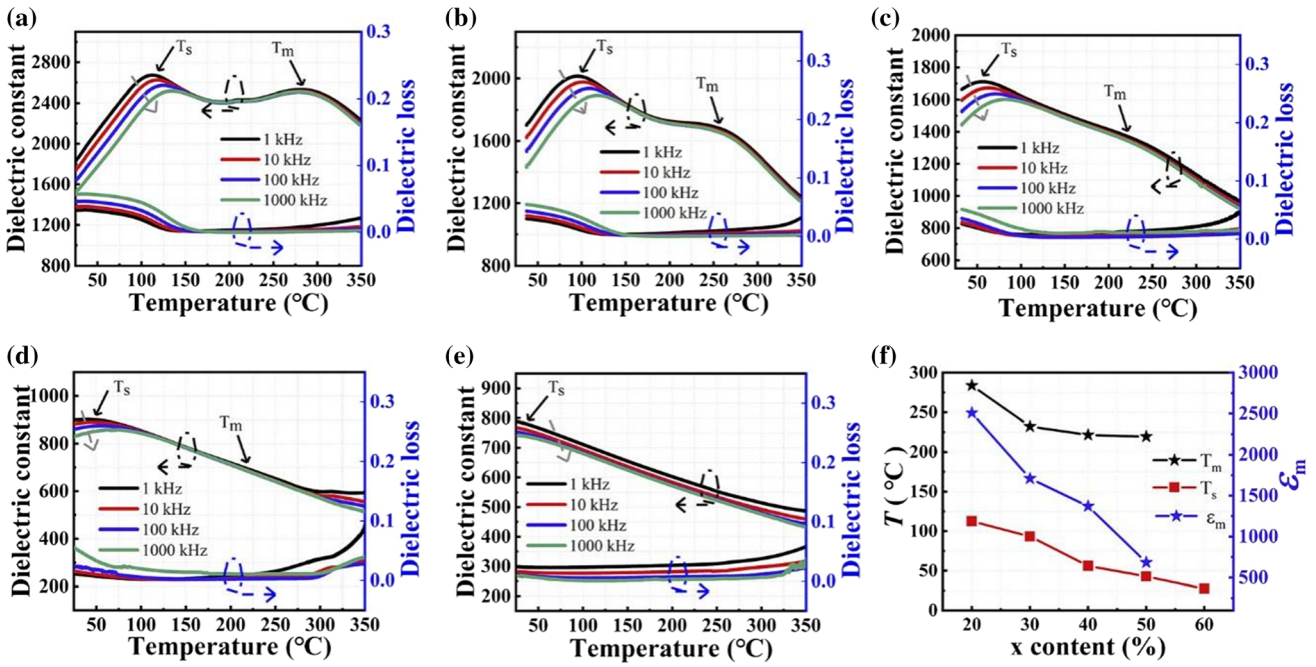

Figure 4 Temperature dependence of dielectric constant and dielectric loss at different frequencies: (**a**) $x = 0.2$, (**b**) $x = 0.3$, (**c**) $x = 0.4$ (**d**) $x = 0.5$, (**e**) $x = 0.6$; (**f**) T_s, T_m and ε_m of (1-x)NBT-xSNT.

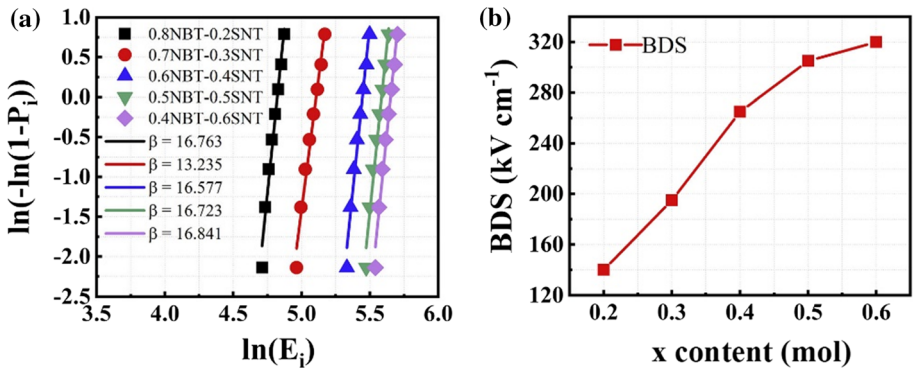

Figure 5 (**a**) Weibull distribution function of BDS; (**b**) the calculated BDS value for the (1-x) NBT-xSNT ceramics.

$$BDS = \frac{1}{G} \tag{3}$$

The higher BDS values are due to their good insulated property, which may be attributed to the decrease of grain size [32].

The total energy-storage density (W_{tot}), W_{rec} and η of (1-x)NBT-xSNT ceramics were calculated according to the P–E hysteresis loops. The P-E hysteresis loops of (1-x)NBT-xSNT ceramics as a function of electric field are illustrated in Fig. 6a. Clearly, the P_{max} and P_r of (1-x)NBT-xSNT ceramics gradually decrease with the content of SNT increasing. The decrease of P_{max} might be ascribed to translation between the weakly polar phase and polar phase [16].

The P_r might be determined the amount of irreversible electric dipoles without external electric field, the amount of irreversible electric dipoles largely depended on the PNRs and grain size [46, 47]. The W_{tot}, W_{rec} and η of (1-x)NBT-xSNT ceramics are summarized, as displayed in Fig. 6b. The η of (1-x)NBT-xSNT ceramics increases significantly from 61 to 88%, when the SNT content increases from 0.2 to 0.6. Particularly, the 0.5NBT-0.5SNT ceramic possesses the highest W_{tot} (4.52 J cm^{-3}) and W_{rec} (3.85 J cm^{-3}) and maintains a relatively high η (85.2%).

To further clarify the energy-storage performance of 0.5NBT-0.5SNT ceramic, the P-E hysteresis loops of under varying electric fields at RT and 10 Hz are

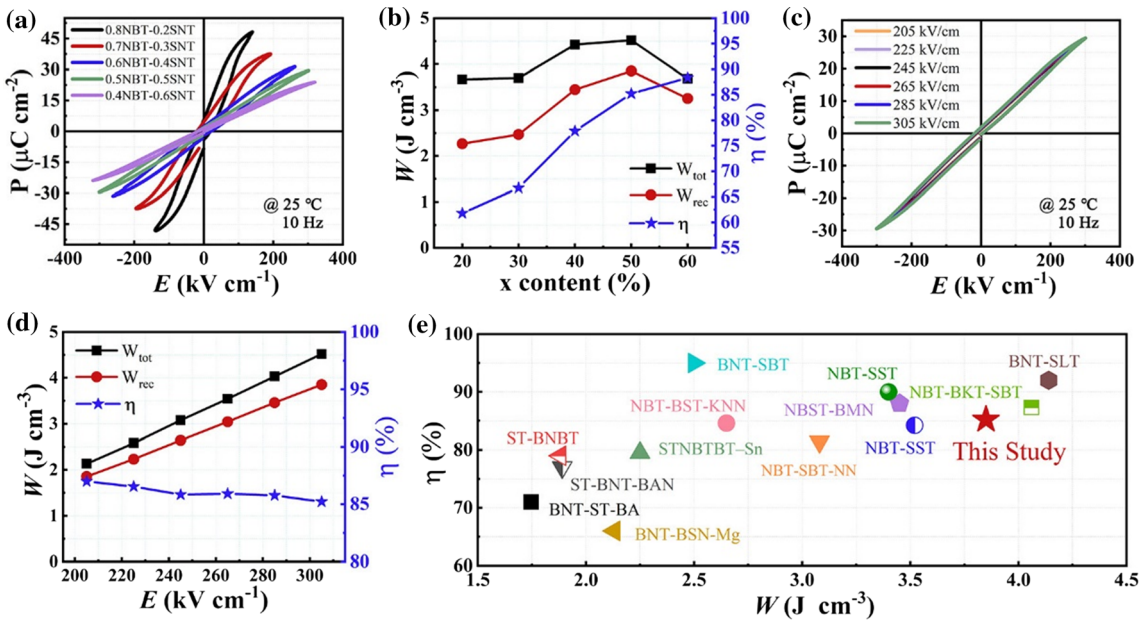

Figure 6 (**a**) P-E loops of (1-x)NBT-xSNT ceramics; (**b**) energy-storage density and efficiency as a function of x content; (**c**) P-E loops under an increasing applied electric field of 0.5NBT-0.5SNT ceramics; (**d**) charge energy density, discharge energy density and energy efficiency as a function of electric field for 0.5NBT-0.5SNT ceramics; (**e**) W_{rec} and η of 0.5NBT-0.5SNT ceramic and previously reported NBT-based ceramics.

shown in Fig. 6c. As electric field increase from 205 to 305 kV cm^{-1}, P_{max} increases from 20 to 29 μC cm^{-2}. The enhanced P_{max} and BDS are conducive to achieving large W_{rec} in 0.5NBT-0.5SNT ceramic. The W_{tot}, W_{rec} and η of 0.5NBT-0.5SNT ceramic under different applied electric fields, respectively, shown in Fig. 6d. It can be observed that the W_{tot} and W_{rec} increase from 2.1 J cm^{-3} and 1.9 J cm^{-3} to 4.52 J cm^{-3} and 3.85 J cm^{-3}, respectively. The η slightly decreases from 87.5 to 85.2% with the BDS increasing due to the enhanced conductivity. For better evaluation of the energy-storage performance of (1-x)NBT-xSNT, a comparison of the energy-storage performance between 0.5NBT-0.5SNT ceramic and other NBT-based ceramics are given in Fig. 6e [2, 22, 23, 26, 28, 30, 31, 35, 48–52]. We can find that the W_{rec} and η of most NBT-based ceramics are less than 3 J cm^{-3} and 80%, respectively.

Figure 7a shows temperature dependence of P-E hysteresis loops for the 0.5NBT-0.5SNT ceramic in the range from 20 to 120 °C at 10 Hz and 200 kV cm^{-1}. All of the P-E hysteresis loops exhibit extremely slim profile. The temperature dependence of W_{loss}, W_{rec} and η of the 0.5NBT-0.5SNT ceramic is summarized in Fig. 7b. A satisfactory thermal stability was observed in the 0.5NBT-0.5SNT ceramic, the variation of the W_{rec} was less than 10% at the test temperature range. Figure 7c shows the P–E hysteresis loops under the applied electric field of 200 kV cm^{-1} in a frequency range of 20–180 Hz. It can be clearly seen that the P–E hysteresis loops are almost unchanged. Figure 7d shows the changing trend of W_{loss}, W_{rec} and η at different frequencies. Correspondingly, the change rates of the W_{rec} and η are below 10%. According to the above analyses suggests that the 0.5NBT-0.5SNT ceramic exhibits excellent energy-storage performance in a wide temperature and frequency range.

To investigate the actual energy-storage performance of the 0.5NBT-0.5SNT ceramic, a pulsed discharge method is utilized to obtain the discharge energy density. The overdamped discharge current curves under different electric fields are shown in Fig. 8a. The pulsed discharged energy density (W_{dis}) can be calculated as: [13, 34, 35]

$$W_{dis} = \frac{R\int i^2(t)}{V}dt \quad (4)$$

where $i(t)$, R and V are the current, load resistance (200 Ω) and the volume of the ceramic, respectively. The time dependence of W_{dis} under different applied electric fields is calculated, as shown in Fig. 8b. The W_{dis} increased from 0.17 J cm^{-3} at 50 kV cm^{-1} to

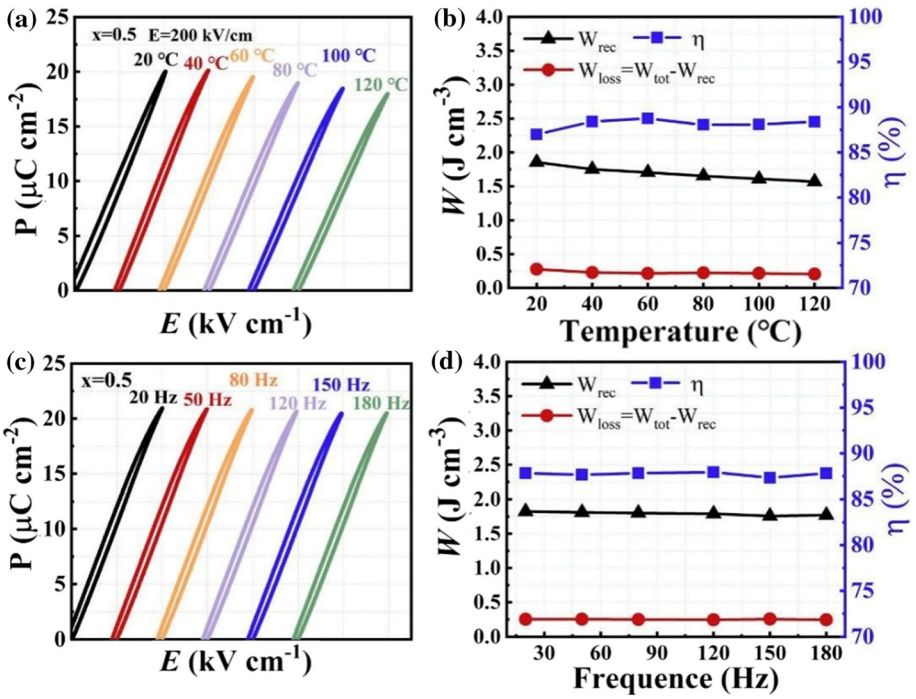

Figure 7 The 0.5NBT-0.5SNT ceramic sample corresponds to the temperature stability and frequency stability under the test conditions.

2.03 J cm^{-3} at 250 kV cm^{-1}. The parameter $t_{0.9}$ (the discharge time that reaches 90% saturated W_{dis} value) of 0.5NBT-0.5SNT ceramic is only 136 ns under the condition of 250 kV cm^{-1}, showing an extremely fast discharge speed. Figure 8c shows the pulse discharge current was measured with a load resistance of zero in the underdamped state. It can be found that the amplitude of the first peak current (I_{max}) gradually increases with the increase of the electric field. The maximum value is 10.6 A when the applied electric field of 250 kV cm^{-1}. It shows that the ceramic has stable discharge behavior.

The current density (C_D) and power density (P_D) of 0.5NBT-0.5SNT ceramic are calculated by the following formulas [23]:

$$C_D = \frac{I_{\max}}{S} \tag{5}$$

$$P_D = \frac{EI_{\max}}{2S} \tag{6}$$

where S and E represent the effective electrode area and the applied electric field, respectively. Related C_D and P_D also show a similar increasing trend as I_{max}, as shown in Fig. 8d. C_D and P_D reach the maximum value of 1401 A cm^{-2} and 175 MW cm^{-3}, respectively, which are better than many energy-storage ceramics.

In addition, it is necessary to consider the stability of charge–discharge performances at different working temperatures. Figure 8e–f displays the discharge current curves of the 0.5NBT-0.5SNT ceramic at 150 kV cm^{-1} from 30 to 120 °C. It is obvious that the W_{dis} was no significant change and $t_{0.9}$ fluctuates between 37 and 43 ns from 30 to 120 °C. Thus, the 0.5NBT-0.5SNT ceramic has a fast discharge speed and an extremely temperature stability over a wide temperature range. Figure 8g shows the underdamped discharge waveforms of the 0.5NBT-0.5SNT ceramic under the different working temperatures. The variation of C_D and P_D is less than 10% over a broad temperature range from 20 to 120 °C. To further describe the advancement of charge–discharge properties, this work and other reported NBT-based ceramics are performed in Fig. 8i. The 0.5NBT-0.5SNT ceramic possesses high C_D and P_D, which is which is superior to most previously reported results [16, 27, 28, 30, 31, 33, 53, 54]. Therefore, 0.5NBT-0.5SNT ceramic has an excellent charge–discharge performance with fast discharge rate, large C_D and P_D, which also indicates that it has great potential in practical applications.

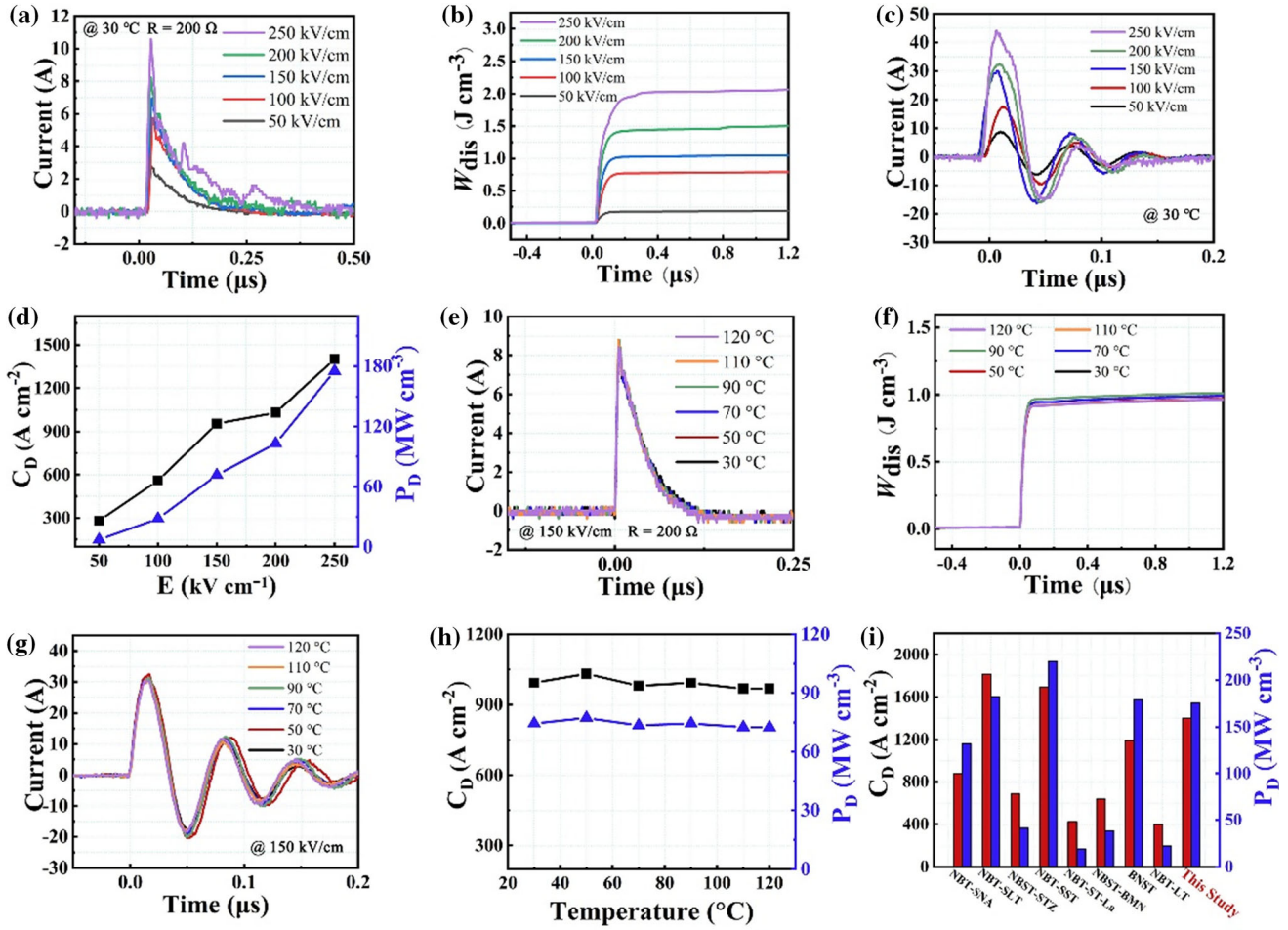

Figure 8 (**a**–**b**) Overdamped discharge current waveform and the electric field strength of 0.5NBT-0.5SNT ceramics under different electric fields; (**c**–**d**) underdamped discharge current waveform and the corresponding current density and power density under different electric fields; (**e**–**f**) overdamped discharge current waveform and the electric field strength of 0.5NBT-0.5SNT ceramics under different temperature; (**g**) underdamped discharge current waveform, the corresponding current density and power density under different temperature; (**i**) contrast of charge–discharge performance of 0.5NBT-0.5SNT ceramic and previously reported NBT-based ceramics.

Conclusions

In summary, the lead-free (1-x)NBT-xSNT ceramics were fabricated by the tape-casting method, and the energy-storage properties and charge–discharge characteristics of the ceramics were studied. The (1-x)NBT-xSNT ceramics exhibit pure perovskite structure and dense structure. It is found that SNT plays a key role in decreasing grain size and domain size, leading to the enhanced BDS and relaxation characteristics. The 0.5NBT-0.5SNT ceramic obtained the highest W_{rec} of 3.85 J cm^{-3} together with a high η of 85.2%. Moreover, the 0.5NBT-0.5SNT ceramic exhibits good temperature stability and frequency stability. In addition, an ultrahigh P_D of 175 MW cm^{-3} and a giant C_D of 1401A cm^{-2} are acquired in the ceramic. These excellent performances prove the great potential of the studied ceramics for dielectric capacitors, promoting the development of advanced power electronic devices and pulsed power system.

Acknowledgements

This work was supported by the Major Program for Science and Technology of Inner Mongolia Autonomous Region (grant No. 2019ZD12), the Program for "Grassland Talents" Innovation Team of Inner Mongolia (Rare Earth Modified Lead-free Ferroelectric Multilayer Ceramic Capacitors Innovative Talent

Team) and Scientific and Technological Development Foundation of the Central Guidance Local (2021ZY0008)

Declarations

Conflict of interest The authors declare that they have no known competing financial interests or personal relationships that could have appeared to influence the work reported in this paper.

References

[1] Palneedi H, Peddigari M, Hwang G-T, Jeong D-Y, Ryu J (2018) High-performance dielectric ceramic films for energy storage capacitors: progress and outlook. Adv Funct Mater. https://doi.org/10.1002/adfm.201803665

[2] Pan Z, Hu D, Zhang Y, Liu J, Shen B, Zhai J (2019) Achieving high discharge energy density and efficiency with NBT-based ceramics for application in capacitors. J Mater Chem C 7:4072–4078. https://doi.org/10.1039/c9tc00087a

[3] Wang D, Fan Z, Zhou D, Khesro A, Murakami S, Feteira A, Zhao Q, Tan X, Reaney IM (2018) Bismuth ferrite-based lead-free ceramics and multilayers with high recoverable energy density. J Mater Chem A 6:4133–4144. https://doi.org/10.1039/c7ta09857j

[4] Zhang H, Wei T, Zhang Q, Ma W, Fan P, Salamon D, Zhang S-T, Nan B, Tan H, Ye Z-G (2020) A review on the development of lead-free ferroelectric energy-storage ceramics and multilayer capacitors. J Mater Chem C 8:16648–16667. https://doi.org/10.1039/d0tc04381h

[5] Zhao L, Liu Q, Gao J, Zhang S, Li JF (2017) Lead-free antiferroelectric silver niobate tantalate with high energy storage performance. Adv Mater. https://doi.org/10.1002/adma.201701824

[6] Chen H, Cong TN, Yang W, Tan C, Li Y, Ding Y (2009) Progress in electrical energy storage system: a critical review. Prog Nat Sci 19:291–312. https://doi.org/10.1016/j.pnsc.2008.07.014

[7] Cao MS, Wang XX, Zhang M, Shu JC, Cao WQ, Yang HJ, Fang XY, Yuan J (2019) Electromagnetic response and energy conversion for functions and devices in low-dimensional materials. Adv Funct Mater. https://doi.org/10.1002/adfm.201807398

[8] Zhang M, Cao M-S, Shu J-C, Cao W-Q, Li L, Yuan J (2021) Electromagnetic absorber converting radiation for multifunction. Mater Sci Eng R Rep. https://doi.org/10.1016/j.mser.2021.100627

[9] Cao M, Wang X, Cao W, Fang X, Wen B, Yuan J (2018) Thermally driven transport and relaxation switching self-powered electromagnetic energy conversion. Small. https://doi.org/10.1002/smll.201800987

[10] Jo W, Dittmer R, Acosta M, Zang J, Groh C, Sapper E, Wang K, Rödel J (2012) Giant electric-field-induced strains in lead-free ceramics for actuator applications – status and perspective. J Electroceram 29:71–93. https://doi.org/10.1007/s10832-012-9742-3

[11] Veerapandiyan V, Benes F, Gindel T, Deluca M (2020) Strategies to improve the energy storage properties of perovskite lead-free relaxor ferroelectrics: a rev. Mater (Basel). https://doi.org/10.3390/ma13245742

[12] Zhou M, Liang R, Zhou Z, Dong X (2018) Novel BaTiO3-based lead-free ceramic capacitors featuring high energy storage density, high power density, and excellent stability. J Mater Chem C 6:8528–8537. https://doi.org/10.1039/c8tc03003k

[13] Qi H, Zuo R (2019) Linear-like lead-free relaxor antiferroelectric $(Bi_{0.5}Na_{0.5})TiO_3$–$NaNbO_3$ with giant energy-storage density/efficiency and super stability against temperature and frequency. J Mater Chem A 7:3971–3978. https://doi.org/10.1039/c8ta12232f

[14] Yang H, Liu P, Yan F, Lin Y, Wang T (2019) A novel lead-free ceramic with layered structure for high energy storage applications. J Alloys Compd 773:244–249. https://doi.org/10.1016/j.jallcom.2018.09.252

[15] Wang W, Pu Y, Guo X, Ouyang T, Shi Y, Yang M, Li J, Shi R, Liu G (2019) Enhanced energy storage properties of lead-free $(Ca_{0.5}Sr_{0.5})_{1-1.5x}La_xTiO_3$ linear dielectric ceramics within a wide temperature range. Ceram Int 45:14684–14690. https://doi.org/10.1016/j.ceramint.2019.04.188

[16] Zhang L, Pu Y, Chen M, Wei T, Peng X (2020) Novel $Na_{0.5}Bi_{0.5}TiO_3$ based, lead-free energy storage ceramics with high power and energy density and excellent high-temperature stability. Chem Eng J. https://doi.org/10.1016/j.cej.2019.123154

[17] Chen L, Wang H, Zhao P, Zhu C, Cai Z, Cen Z, Li L, Wang X (2019) Multifunctional $BaTiO_3$-$(Bi_{0.5}Na_{0.5})TiO_3$-based MLCC with high-energy storage properties and temperature stability. J Am Ceram Soc 102:4178–4187. https://doi.org/10.1111/jace.16292

[18] Wang G, Lu Z, Li J, Ji H, Yang H, Li L, Sun S, Feteira A, Yang H, Zuo R, Wang D, Reaney IM (2020) Lead-free (Ba, Sr)Ti_O3-BiFe_O3 based multilayer ceramic capacitors with high energy density. J Eur Ceram Soc 40:1779–1783. https://doi.org/10.1016/j.jeurceramsoc.2019.12.009

[19] Qu N, Du H, Hao X (2019) A new strategy to realize high comprehensive energy storage properties in lead-free bulk ceramics. J Mater Chem C 7:7993–8002. https://doi.org/10.1039/c9tc02088h

[20] Meng X, Zhao Y, Li Y, Hao X (2021) Simultaneously achieving ultrahigh energy density and power density in $PbZrO_3$-based antiferroelectric ceramics with field-induced multistage phase transition. J Alloys Compd. https://doi.org/10.1016/j.jallcom.2021.159149

[21] Liu X, Zhao Y, Sun N, Li Y, Hao X (2021) Ultra-high energy density induced by diversified enhancement effects in $(Pb_{0.98}-xLa_{0.02}Cax)(Zr_{0.7}Sn0.3)_{0.995}O_3$ antiferroelectric multilayer ceramic capacitors. Chem Eng J. https://doi.org/10.1016/j.cej.2020.128032

[22] Li J, Li F, Xu Z, Zhang S (2018) Multilayer lead-free ceramic capacitors with ultrahigh energy density and efficiency. Adv Mater 30,1802155:1-7. https://doi.org/10.1002/adma.201802155

[23] Wu Y, Fan Y, Liu N, Peng P, Zhou M, Yan S, Cao F, Dong X, Wang G (2019) Enhanced energy storage properties in sodium bismuth titanate-based ceramics for dielectric capacitor applications. J Mater Chem C 7:6222–6230. https://doi.org/10.1039/c9tc01239g

[24] Butnoi P, Manotham S, Jaita P, Randorn C, Rujijanagul G (2018) High thermal stability of energy storage density and large strain improvement of lead-free Bi0.5(Na0.40K0.10)-TiO3 piezoelectric ceramics doped with La and Zr. J Eur Ceram Soc 38:3822–3832. https://doi.org/10.1016/j.jeurceramsoc.2018.04.024

[25] Le PG, Fisher JG, Moon WJ (2019) Effect of composition on the growth of single crystals of $(1–x)(Na_{1/2}Bi_{1/2})TiO_3$-$xSrTiO_3$ by solid state crystal growth. Mater (Basel). https://doi.org/10.3390/ma12152357

[26] Hu D, Pan Z, Zhang X, Ye H, He Z, Wang M, Xing S, Zhai J, Fu Q, Liu J (2020) Greatly enhanced discharge energy density and efficiency of novel relaxation ferroelectric BNT–BKT-based ceramics. J Mater Chem C 8:591–601. https://doi.org/10.1039/c9tc05528b

[27] Yan F, Zhou X, He X, Bai H, Wu S, Shen B, Zhai J (2020) Superior energy storage properties and excellent stability achieved in environment-friendly ferroelectrics via composition design strategy. Nano Energy. https://doi.org/10.1016/j.nanoen.2020.105012

[28] Qiao X, Zhang F, Wu D, Chen B, Zhao X, Peng Z, Ren X, Liang P, Chao X, Yang Z (2020) Superior comprehensive energy storage properties in $Bi_{0.5}Na_{0.5}TiO_3$-based relaxor ferroelectric ceramics. Chem Eng J. https://doi.org/10.1016/j.cej.2020.124158

[29] Yang Y, Wang H, Bi L, Zheng Q, Fan G, Jie W, Lin D (2019) High energy storage density and discharging efficiency in La^{3+}/Nb^{5+}-co-substituted $(Bi_{0.5}Na_{0.5})_{0.94}Ba_{0.06}TiO_3$ ceramics. J Eur Ceram Soc 39:3051–3056. https://doi.org/10.1016/j.jeurceramsoc.2019.04.031

[30] Lin Y, Li D, Zhang M, Yang H (2020) $(Na_{0.5}Bi_{0.5})_{0.7}$-$Sr_{0.3}TiO_3$ modified by $Bi(Mg_{2/3}Nb_{1/3})O_3$ ceramics with high energy-storage properties and an ultrafast discharge rate. J Mater Chem C 8:2258–2264. https://doi.org/10.1039/c9tc06218a

[31] Qiao X, Sheng A, Wu D, Zhang F, Chen B, Liang P, Wang J, Chao X, Yang Z (2021) A novel multifunctional ceramic with photoluminescence and outstanding energy storage properties. Chem Eng J. https://doi.org/10.1016/j.cej.2020.127368

[32] Liu X, Yang T, Gong W (2021) Comprehensively enhanced energy-storage properties in $(Pb1-3x/2Lax)(Zr_{0.995}Ti_{0.005})$-$O_3$ antiferroelectric ceramics via composition optimization. J Mater Chem C. https://doi.org/10.1039/d1tc02972j

[33] Yan F, Huang K, Jiang T, Zhou X, Shi Y, Ge G, Shen B, Zhai J (2020) Significantly enhanced energy storage density and efficiency of BNT-based perovskite ceramics via A-site defect engineering. Energy Stor Mater 30:392–400. https://doi.org/10.1016/j.ensm.2020.05.026

[34] Li Q, Wang J, Liu Z, Dong G, Fan H (2015) Enhanced energy-storage properties of BaZrO3-modified $0.80Bi_{0.5}$-$Na_{0.5}TiO_3$–$0.20Bi_{0.5}K_{0.5T}iO_3$ lead-free ferroelectric ceramics. J Mater Sci 51:1153–1160. https://doi.org/10.1007/s10853-015-9446-6

[35] Shi P, Zhu L, Gao W, Yu Z, Lou X, Wang X, Yang Z, Yang S (2019) Large energy storage properties of lead-free $(1–x)(0.72Bi_{0.5}Na_{0.5}TiO_3$-$0.28SrTiO_3)$-$xBiAlO_3$ ceramics at broad temperature range. J Alloys Compd 784:788–793. https://doi.org/10.1016/j.jallcom.2019.01.077

[36] Qiao X, Wu D, Zhang F, Niu M, Chen B, Zhao X, Liang P, Wei L, Chao X, Yang Z (2019) Enhanced energy density and thermal stability in relaxor ferroelectric $Bi_{0.5}Na_{0.5}TiO_3$-$Sr_{0.7}Bi_{0.2}TiO_3$ ceramics. J Eur Ceram Soc 39:4778–4784. https://doi.org/10.1016/j.jeurceramsoc.2019.07.003

[37] Zheng P, Zhang JL, Tan YQ, Wang CL (2012) Grain-size effects on dielectric and piezoelectric properties of poled $BaTiO_3$ ceramics. Acta Mater 60:5022–5030. https://doi.org/10.1016/j.actamat.2012.06.015

[38] Li Y, Sun N, Du J, Li X, Hao X (2019) Stable energy density of a PMN–PST ceramic from room temperature to its Curie point based on the synergistic effect of diversified energy. J Mater Chem C 7:7692–7699. https://doi.org/10.1039/c9tc02172h

[39] Sun N, Li Y, Liu X, Hao X (2020) High energy-storage density under low electric field in lead-free relaxor ferroelectric film based on synergistic effect of multiple polar structures. J Power Sour. https://doi.org/10.1016/j.jpowsour.2019.227457

[40] Zhang L, Wang Z, Li Y, Chen P, Cai J, Yan Y, Zhou Y, Wang D, Liu G (2019) Enhanced energy storage performance in Sn

doped Sr0.6(Na0.5Bi0.5)0.4TiO3 lead-free relaxor ferroelectric ceramics. J Eur Ceram Soc 39:3057–3063. https://doi.org/10.1016/j.jeurceramsoc.2019.02.004

[41] Xu Q, Lanagan MT, Huang X, Xie J, Zhang L, Hao H, Liu H (2016) Dielectric behavior and impedance spectroscopy in lead-free BNT–BT–NBN perovskite ceramics for energy storage. Ceram Int 42:9728–9736. https://doi.org/10.1016/j.ceramint.2016.03.062

[42] Li Q, Yao Z, Ning L, Gao S, Hu B, Dong G, Fan H (2018) Enhanced energy-storage properties of (1–x)($0.7Bi_{0.5}Na_{0.5}TiO_3$-$0.3Bi_{0.2}Sr_{0.7}TiO_3$)-x$NaNbO_3$ lead-free ceramics. Ceram Int 44:2782–2788. https://doi.org/10.1016/j.ceramint.2017.11.018

[43] Yang H, Yan F, Lin Y, Wang T (2018) Enhanced energy-storage properties of lanthanum-doped $Bi_{0.5}Na_{0.5}TiO_3$-based lead-free ceramics. Energy Technol 6:357–365. https://doi.org/10.1002/ente.201700504

[44] Gao F, Dong X, Mao C, Liu W, Zhang H, Yang L, Cao F, Wang G, Jones J (2011) Energy-storage properties of $0.89Bi_{0.5}Na_{0.5}TiO_3$-$0.06BaTiO_3$-$0.05K_{0.5}Na_{0.5}NbO_3$ lead-free anti-ferroelectric ceramics. J Am Ceram Soc 94:4382–4386. https://doi.org/10.1111/j.1551-2916.2011.04731.x

[45] Liu X, Shi J, Zhu F, Du H, Li T, Liu X, Lu H (2018) Ultrahigh energy density and improved discharged efficiency in bismuth sodium titanate based relaxor ferroelectrics with A-site vacancy. J Mater 4:202–207. https://doi.org/10.1016/j.jmat.2018.05.006

[46] Jin L, Li F, Zhang S, Green DJ (2014) Decoding the fingerprint of ferroelectric loops: comprehension of the material properties and structures. J Am Ceram Soc 97:1–27. https://doi.org/10.1111/jace.12773

[47] Zhang L, Zhao C, Zheng T, Wu J (2020) Large electrocaloric effect in $(Bi_{0.5}Na_{0.5})TiO_3$-based relaxor ferroelectrics. ACS Appl Mater Inter 12:33934–33940. https://doi.org/10.1021/acsami.0c09343

[48] Cui C, Pu Y (2018) Effect of Sn substitution on the energy storage properties of $0.45SrTiO_3$–$0.2Na_{0.5}Bi_{0.5}TiO_3$–$0.35BaTiO_3$ ceramics. J Mater Sci 53:9830–9841. https://doi.org/10.1007/s10853-018-2282-8

[49] Zhang L, Pu Y, Chen M, Liu G (2018) Antiferroelectric-like properties in MgO-modified $0.775Na_{0.5}Bi_{0.5}TiO_3$-$0.225BaSnO_3$ ceramics for high power energy storage. J Eur Ceram Soc 38:5388–5395. https://doi.org/10.1016/j.jeurceramsoc.2018.08.010

[50] Yang L, Kong X, Cheng Z, Zhang S (2019) Ultra-high energy storage performance with mitigated polarization saturation in lead-free relaxors. J Mater Chem A 7:8573–8580. https://doi.org/10.1039/c9ta01165j

[51] Yan F, Yang H, Lin Y, Wang T (2017) Dielectric and ferroelectric properties of SrTiO3-$Bi_{0.5}Na_{0.5}TiO_3$-$BaAl_{0.5}Nb_{0.5}O_3$ lead-free ceramics for high-energy-storage applications. Inorg Chem 56:13510–13516. https://doi.org/10.1021/acs.inorgchem.7b02181

[52] Wang C, Yan F, Yang H, Lin Y, Wang T (2018) Dielectric and ferroelectric properties of $SrTiO_3$-$Bi_{0.54}Na_{0.46}TiO_3$-$BaTiO_3$ lead-free ceramics for high energy storage applications. J Alloys Compd 749:605–611. https://doi.org/10.1016/j.jallcom.2018.03.195

[53] Li D, Lin Y, Zhang M, Yang H (2020) Achieved ultrahigh energy storage properties and outstanding charge–discharge performances in $(Na0.5Bi_{0.5})_{0.7}Sr_{0.3}TiO_3$-based ceramics by introducing a linear additive. Chem Eng J. https://doi.org/10.1016/j.cej.2019.123729

[54] Liu G, Hu L, Wang Y, Wang Z, Yu L, Lv J, Dong J, Wang Y, Tang M, Guo B, Yu K, Yan Y (2020) Investigation of electrical and electric energy storage properties of La-doped $Na_{0.3}Sr_{0.4}Bi_{0.3}TiO_3$ based Pb-free ceramics. Ceram Int 46:19375–19384. https://doi.org/10.1016/j.ceramint.2020.04.280